ADVANCED MATERIALS INTERFACES
www.advmatinterfaces.de

Fe_2O_3–TiO_2 Nano-heterostructure Photoanodes for Highly Efficient Solar Water Oxidation

Davide Barreca, Giorgio Carraro, Alberto Gasparotto, Chiara Maccato, Michael E. A. Warwick, Kimmo Kaunisto,* Cinzia Sada, Stuart Turner, Yakup Gönüllü, Tero-Petri Ruoko, Laura Borgese, Elza Bontempi, Gustaaf Van Tendeloo, Helge Lemmetyinen, and Sanjay Mathur*

Harnessing solar energy for the production of clean hydrogen by photoelectrochemical water splitting represents a very attractive, but challenging approach for sustainable energy generation. In this regard, the fabrication of Fe_2O_3–TiO_2 photoanodes is reported, showing attractive performances [≈2.0 mA cm^{-2} at 1.23 V vs. the reversible hydrogen electrode in 1 M NaOH] under simulated one-sun illumination. This goal, corresponding to a tenfold photoactivity enhancement with respect to bare Fe_2O_3, is achieved by atomic layer deposition of TiO_2 over hematite (α-Fe_2O_3) nanostructures fabricated by plasma enhanced-chemical vapor deposition and final annealing at 650 °C. The adopted approach enables an intimate Fe_2O_3–TiO_2 coupling, resulting in an electronic interplay at the Fe_2O_3/TiO_2 interface. The reasons for the photocurrent enhancement determined by TiO_2 overlayers with increasing thickness are unraveled by a detailed chemico-physical investigation, as well as by the study of photogenerated charge carrier dynamics. Transient absorption spectroscopy shows that the increased photoelectrochemical response of heterostructured photoanodes compared to bare hematite is due to an enhanced separation of photogenerated charge carriers and more favorable hole dynamics for water oxidation. The stable responses obtained even in simulated seawater provides a feasible route in view of the eventual large-scale generation of renewable energy.

1. Introduction

The development of sustainable energy production systems has become an ever-growing demand under the rising stress of the global population, living standards, and increased industrialization.[1–7] In this context, photoactivated methods such as photoelectrochemical (PEC) H_2O splitting, starting from two abundant natural resources such as solar photons and water, are environmentally benign approaches for the production of hydrogen as a clean and renewable energy vector.[8–24] A key issue for PEC water splitting is the identification of suitable photoanode materials satisfying the challenging requirements for solar hydrogen generation.[13,14,25,26] Among the most promising candidates, hematite (α-Fe_2O_3) has long been a preferred choice[18,20,27–32] thanks to its good photochemical stability, earth abundance, nontoxicity, low cost and proper band gap ($E_G \approx 2.1$ eV) to absorb a large fraction of the solar spectrum.[3,4,16,21,33–36] In spite of these advantages, the solar-to-hydrogen

Dr. D. Barreca
CNR-IENI and INSTM
Department of Chemistry
Padova University
35131 Padova, Italy
E-mail: davide.barreca@unipd.it
Dr. G. Carraro, Dr. A. Gasparotto, Prof. C. Maccato, Dr. M. E. A. Warwick
Department of Chemistry
Padova University and INSTM
35131 Padova, Italy
Dr. K. Kaunisto, T.-P. Ruoko, Prof. H. Lemmetyinen
Department of Chemistry and Bioengineering
Tampere University of Technology
33101 Tampere, Finland
E-mail: kimmo.kaunisto@tut.fi

DOI: 10.1002/admi.201500313

Prof. C. Sada
Department of Physics and Astronomy
Padova University
35131 Padova, Italy
Dr. S. Turner, Prof. G. Van Tendeloo
EMAT
University of Antwerp
2020 Antwerpen, Belgium
Dr. Y. Gönüllü, Prof. S. Mathur
Department of Chemistry
Chair of Inorganic and Materials Chemistry
Cologne University
50939 Cologne, Germany
Dr. L. Borgese, Prof. E. Bontempi
Chemistry for Technologies Laboratory
University of Brescia
25123 Brescia, Italy

efficiency of hematite falls well short of the theoretical maximum value (≈13%)[6,7,10,11,34,37] due to a number of factors,[2,12,17,25,30,38] including poor charge transport properties, improper band positions for unassisted water splitting, low electron–hole pair lifetime (<10 ps), and small exciton diffusion length (≈2–4 nm).[11,28,35,39,40] To overcome these drawbacks and enhance hematite conductivity and photoresponses, the most commonly used strategies are nanoarchitecture engineering[7,11,18,22,26,39] and elemental doping.[17,25,29,41,42] Other improvements have been afforded by the introduction of oxygen evolution catalysts (OECs), such as Co-, Ni-, Ir-, and Ru-based ones.[1,10,19,24–26,43] Despite the advantageous reduction in the onset potential, most of these systems are toxic and/or expensive, being unsuitable for large-scale energy production. In addition, water oxidation efficiencies are often limited by surface recombination, a severe issue to be tackled.[19,26,44] An alternative strategy to address the primary requirements for an efficient solar-to-hydrogen conversion consists in the formation of nano-heterostructures involving Fe_2O_3 coupling with suitable underlayers or overlayers[1,4,33,40,45,46] to suppress electron back recombination at the hematite/substrate interface,[20,28,29] enhance light absorption, and improve charge carrier transport properties.[5,16,19,27,47] So far, several works have been focused on the surface functionalization of Fe_2O_3 nanosystems with various oxides, such as Al_2O_3, Ga_2O_3, $Fe_xSn_{1-x}O_4$, and TiO_2.[3,10,19,20,39] The obtained results highlight the possibility of improving PEC performances by passivation of surface states, protection against corrosion, use of buried semiconductor junctions,[2,19] and a proper tailoring of charge transfer processes between the constituent phases.[20,47] Nevertheless, the practical use of modified hematite photoanodes in efficient, durable, and low-cost solar hydrogen production is still hindered by various factors,[37] including the system stability[29] and the difficulties in identifying precise structure–functions relationships.[6,17] In addition, driving PEC water splitting more efficiently than the state-of-the-art hematite photoanodes[48] remains a main hurdle impeding further technological developments.[34]

In the present study, we report on a method for the enhancement of hematite photoanode charge transfer, resulting in a remarkable improvement of the recorded PEC performances in solar water splitting. In particular, we have devoted our attention to the coating of plasma enhanced-chemical vapor deposition (PE-CVD) hematite nanostructures by an atomic layer deposition (ALD) TiO_2 overlayer, followed by thermal treatment in air at 650 °C. It is worth highlighting that, despite several efforts aimed at investigating Ti incorporation into hematite photoelectrodes,[7,29,35,38,40,42] Fe_2O_3–TiO_2 multilayered and composite systems have so far been much less investigated.[3,6,16,27,45] For these materials, the current density for water photooxidation has been reported to drop off with an increased number of TiO_2 ALD cycles, the reasons underlying this behavior being unclear.[2] In this work, taking advantage of ALD repeatability, conformity, and precise thickness control,[24,46,49] we focus our attention on the PEC behavior of Fe_2O_3–TiO_2 nano-heterostructures characterized by different TiO_2 overlayer thicknesses. A relevant attention is devoted to the interrelations between system properties and functional performances, with particular regard to the structural and electronic interplay occurring at Fe_2O_3/TiO_2 heterointerfaces. Under optimized conditions, a tenfold photocurrent increase compared to bare α-Fe_2O_3 photoanodes was observed, corresponding to the highest performances ever reported for similar systems, especially at high applied potentials. This feature, along with the high stability even in simulated seawater, for which solar splitting has only been seldom investigated,[50] represents an important goal toward the sustainable and efficient conversion of solar light into chemical energy.

2. Results and Discussion

2.1. Preparation and Characterization of Fe_2O_3–TiO_2 Photoanodes

Fe_2O_3–TiO_2 photoanodes were fabricated by a three-step protocol, involving: (i) PE-CVD of Fe_2O_3 on fluorine-doped tin oxide (FTO) substrates; (ii) ALD of TiO_2 with a different cycle number, in order to tailor the corresponding overlayer thickness; and (iii) annealing in air for 1 h at 650 °C (**Table 1**). Bare Fe_2O_3 (hereafter labeled as Fe_2O_3), composed of pure α-Fe_2O_3 (hematite) free from other iron oxide polymorphs, was characterized by an inherently porous nanoorganization [Figure S1, Supporting Information]. The subsequent ALD of TiO_2 resulted in morphological variations, as revealed by field emission-scanning electron microscopy (FE-SEM; see **Figure 1**). In particular, specimens 400_L and 400_H, obtained with a lower and a higher number of ALD cycles, presented more rounded surface features than the pristine Fe_2O_3 (Figure S1a,b, Supporting Information). In the case of 400_L, functionalization with TiO_2 produced only a modest alteration of Fe_2O_3 aggregate features, indicating the formation of a conformal thin film. For specimen 400_H, more marked modifications of the surface morphology took place (Figure 1a,b). The system double-layered structure was clearly evidenced by cross-sectional FE-SEM images (Figure 1c,d). As can be observed, upon going from specimen 400_L to the homologous 400_H, the TiO_2 overlayer thickness underwent a parallel increase. These observations, along with the intimate and uniform Fe_2O_3–TiO_2 contact, highlight the intrinsic ALD conformal coverage capability,[18,19,49] enabling a fine control of the resulting Fe_2O_3–TiO_2 heterojunction features. Cross sectional FE-SEM images enabled the estimation of the total nanodeposit (and titania overlayer) thickness values, yielding 400 ± 15 (35 ± 10) and 480 ± 30 (80 ± 10) nm for 400_L and 400_H, respectively. In order to attain further insight into the system topography, the material surfaces were probed by atomic force microscopy (AFM; Figure 1g,h). The recorded micrographs showed the formation of multigrain structures, in line with FE-SEM observations. Irrespective of the synthesis conditions, very similar root-mean-square (RMS) roughness values (≈20 nm) were obtained for the analyzed systems.

Table 1. Main growth and processing conditions for FTO-supported photoanodes investigated in the present study.

Sample ID	Fe_2O_3 by PE-CVD	TiO_2 by ALD	Thermal annealing
Fe_2O_3	400 °C, 1 h	//	650 °C, 1 h, air
400_L	400 °C, 1 h	150 °C, 1150 cycles	650 °C, 1 h, air
400_H	400 °C, 1 h	150 °C, 5750 cycles	650 °C, 1 h, air

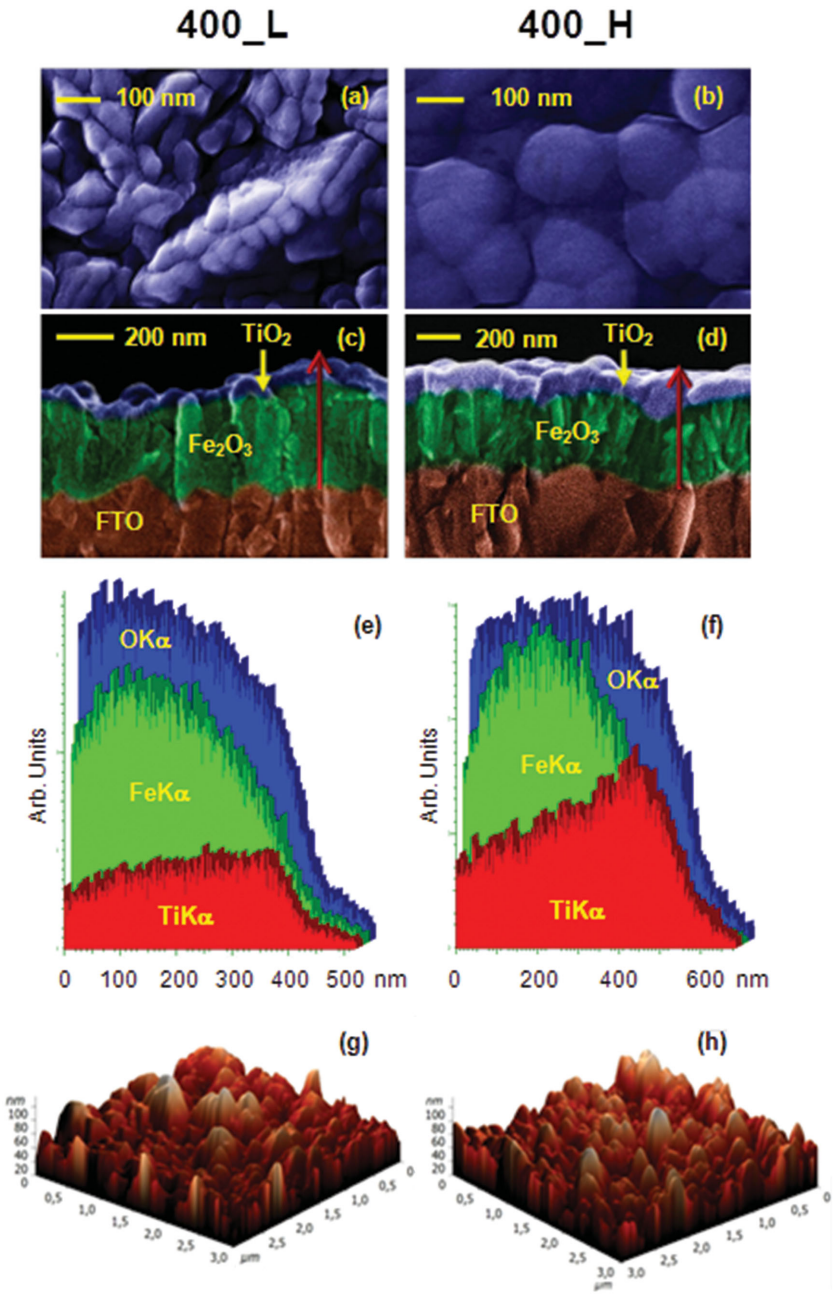

Figure 1. a,b) Plane-view FE-SEM images, c,d) cross-sectional FE-SEM images, e,f) EDXS line-scan profiles recorded along the lines marked in cross-sectional views, and g,h) AFM micrographs for Fe_2O_3–TiO_2 specimens. In (e) and (f), arrows mark the direction of abscissa increase.

The local in-depth composition was analyzed by energy dispersive X-ray spectroscopy (EDXS) line-scans (Figure 1e,f). The obtained data showed that TiO_2 was mainly concentrated in the outermost material region, a phenomenon more evident for the 400_H sample, confirming that a higher number of ALD cycles resulted in a thicker TiO_2 overlayer, as already appreciated by FE-SEM images. Conversely, the FeKα line intensity underwent a progressive increase in the inner system region at the expense of the TiKα one, confirming the predominance of Fe_2O_3 in the deposit regions closer to the FTO substrate.

Since the mutual spatial distribution of Fe_2O_3 and TiO_2 is a key issue for an optimal heterostructure engineering, the in-depth chemical composition along the thickness was further investigated by secondary ion mass spectrometry (SIMS) analyses (**Figure 2** a,b). The obtained data allowed the estimation of a mean C concentration (averaged over the whole thickness) as low as 150 ppm, highlighting thus the purity of the obtained materials. Irrespective of the processing conditions, the O ionic yield remained almost constant throughout the investigated depth. As can be observed in Figure 2, the outermost sample region was Ti-rich, a phenomenon particularly evident for specimen 400_H, characterized by a higher thickness of the TiO_2 overlayer. Upon increasing the sputtering time, a concomitant increase in the Fe ionic yield and a progressive decrease in the Ti one took place, in agreement with EDXS data (see Figure 1). This evidence suggested that the TiO_2 layer was covering hematite nanostructures even in the inner regions, a phenomenon due to the synergy between the Fe_2O_3 porosity and the good conformality achievable by the use of ALD. Finally, both titanium and iron signals underwent a net intensity decrease at the interface with the FTO substrate. The Sn tailing extending into the nanodeposits at the interfacial region suggested the occurrence of tin diffusion from the FTO substrate induced by thermal annealing, at least to some extent. This phenomenon, already observed in previous works, might beneficially contribute to PEC performances, due to an improved system electrical conductivity.[37,43,51]

Overall, the data discussed so far point to the obtainment of Fe_2O_3–TiO_2 heterostructures, with titanium oxide being mainly confined in the outermost system regions. To perform a detailed characterization of the Fe and Ti chemical environments, X-ray photoelectron spectroscopy (XPS) analyses were carried out. Wide-scan XPS spectra (Figure S2a, Supporting Information) were dominated by titanium and oxygen photopeaks. In the case of sample 400_L, the presence of iron could also be detected (see Figure 2d), suggesting in this case the occurrence of a thinner and porous TiO_2 overlayer (compare TEM analysis; see below). Irrespective of the used ALD conditions, the $Ti2p_{3/2}$ binding energy (BE) of 458.5 eV, as well as the separation between the spin-orbit components [Δ(BE) = 5.7 eV] (Figure 2c), was in line with the presence of Ti(IV) in TiO_2.[35,52] The Fe2p peak shape and position [Figure 2d; BE($Fe2p_{3/2}$) = 711.1 eV], along with the pertaining spin-orbit splitting [Δ(BE) = 13.7 eV], were consistent with the formation of iron(III) oxide free from other Fe oxidation states.[7,11,33,35,42,52] The O1s

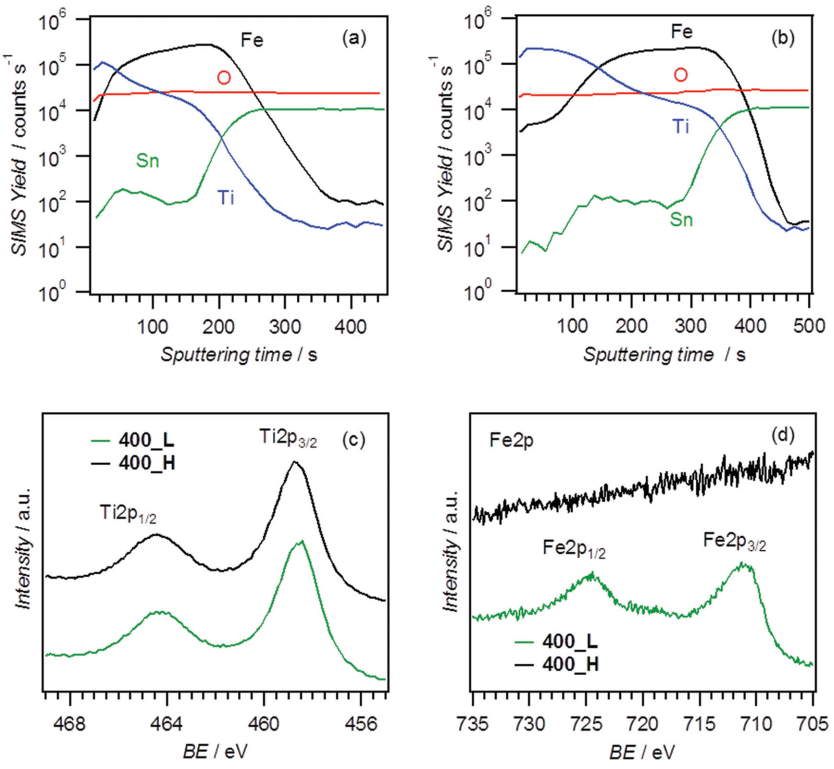

Figure 2. SIMS depth profiles for Fe_2O_3–TiO_2 deposits on FTO: a) 400_L and b) 400_H. c) Ti2p and d) Fe2p XPS surface spectra for the same specimens.

signal (Figure S2b, Supporting Information) could be fitted by two contributing bands located at (I) BE = 530.0 eV and (II) 532.0 eV, attributed to lattice O and surface –OH groups/adsorbed oxygen.[4,7,35,42]

The structure of the deposited Fe_2O_3–TiO_2 photoanodes was investigated by X-ray diffraction (XRD). The recorded patterns (Figure S3, Supporting Information) were dominated by a series of signals corresponding to hematite reflections for both specimens 400_L and 400_H.[53] Interestingly, the latter also showed the appearance of additional peaks at 2θ = 25.3° and 47.9°, related to (101) and (200) crystallographic planes of anatase TiO_2,[54] whereas no signals related to titania could be unambiguously observed for sample 400_L, due to the lower amount of deposited TiO_2 (compare the thickness values obtained by cross-sectional FE-SEM analyses, see above). In accordance with XPS results, no reflections related to Fe–Ti–O ternary phases were present, and the absence of appreciable angular shifts also enabled to rule out the occurrence of Ti doping into Fe_2O_3.

To investigate the nanoscale structure of Fe_2O_3–TiO_2 materials, high resolution transmission electron microscopy (HR-TEM), high angle annular dark field scanning transmission electron microscopy (HAADF-STEM), and EDXS analyses were carried out. **Figure 3**a–d displays HAADF-STEM (*Z* contrast) overview images of both samples in cross-section, together with EDXS elemental maps for Ti, Fe, Sn, and Si, evidencing the glass/FTO/α-Fe_2O_3/TiO_2 multilayer stacks. The Fe_2O_3/TiO_2 interface is imaged in more detail in Figure 3e,f, from which TiO_2 overlayer thickness values were extracted and were in excellent agreement with those provided by FE-SEM analyses (see above and Figure 1). Irrespective of the used ALD conditions, the Fe_2O_3 nanodeposit consisted of well-developed upward growing hematite needles, whose assembly resulted in an open, porous structure. This peculiar texture enabled the ALD TiO_2 coating to be deposited even in the inner system regions, confirming the formation of Fe_2O_3–TiO_2 nano-heterostructures. The overlayers, composed by TiO_2 with the anatase crystal phase, are further imaged by the HR micrographs reported in Figure 3g,h. The presence of small voids (mean size of few nanometers), imaged as a dark contrast in the mass-thickness sensitive HAADF-STEM view in Figure 3h, highlights the porosity of the titania top layer. Electron diffraction (ED) maps of both specimens showed reflections that could be attributed to hematite and anatase phases (see Figure S4, Supporting Information), despite the 400_L sample displaying very weak anatase signals due to the low TiO_2 amount (see also XRD data).

The target Fe_2O_3/TiO_2 nano-heterostructures were also analyzed by optical absorption spectroscopy (Figure S5, Supporting Information). The recorded spectra were characterized by a sub-bandgap scattering tail in the 600–750 nm region and a sharp absorbance increase occurring from 550–600 nm toward lower wavelengths, consistent with the bandgap of hematite.[25,40,43] As a whole, the optical properties of the present Fe_2O_3–TiO_2 heterostructures are appealing for PEC water splitting triggered by solar irradiation, since these photoanodes can efficiently absorb a significant fraction of the Vis spectrum. From Tauc plots, it was possible to extrapolate a mean band gap (E_G) value of 2.1 eV, revealing that the TiO_2 overlayers did not appreciably affect the optical features in the Vis range.[16,17,38,44]

2.2. PEC Investigation of Fe_2O_3–TiO_2 Photoanodes

The functional properties of Fe_2O_3–TiO_2 heterostructures in PEC water splitting were evaluated in NaOH aqueous solutions (**Figure 4**a) and compared with those of a bare Fe_2O_3 photoelectrode. In the absence of illumination, the samples showed very small currents, and even when the water electrolysis reaction was reached at ≈1.8 V,[5] dark currents were lower than 1 mA cm^{-2}. Upon simulated solar illumination, a net *j* increase at potentials lower than E° (1.23 V vs reversible hydrogen electrode (RHE)) took place, since part of the energy required for the oxidation process is captured from the incident light.[5] Considering the onset potentieal (E_{onset}) as the value at which a current density of 0.02 mA cm^{-2} is first reached,[6] for the pure Fe_2O_3 photoanode E_{onset} was estimated to be 1.1 V_{RHE}. Subsequently, a progressive *j* increase with *E* occurred, reaching a value of 0.24 mA cm^{-2} at 1.23 V_{RHE}. As can be observed, the functionalization of hematite with TiO_2 resulted in a decrease of the onset potential and in a significant increase of the recorded

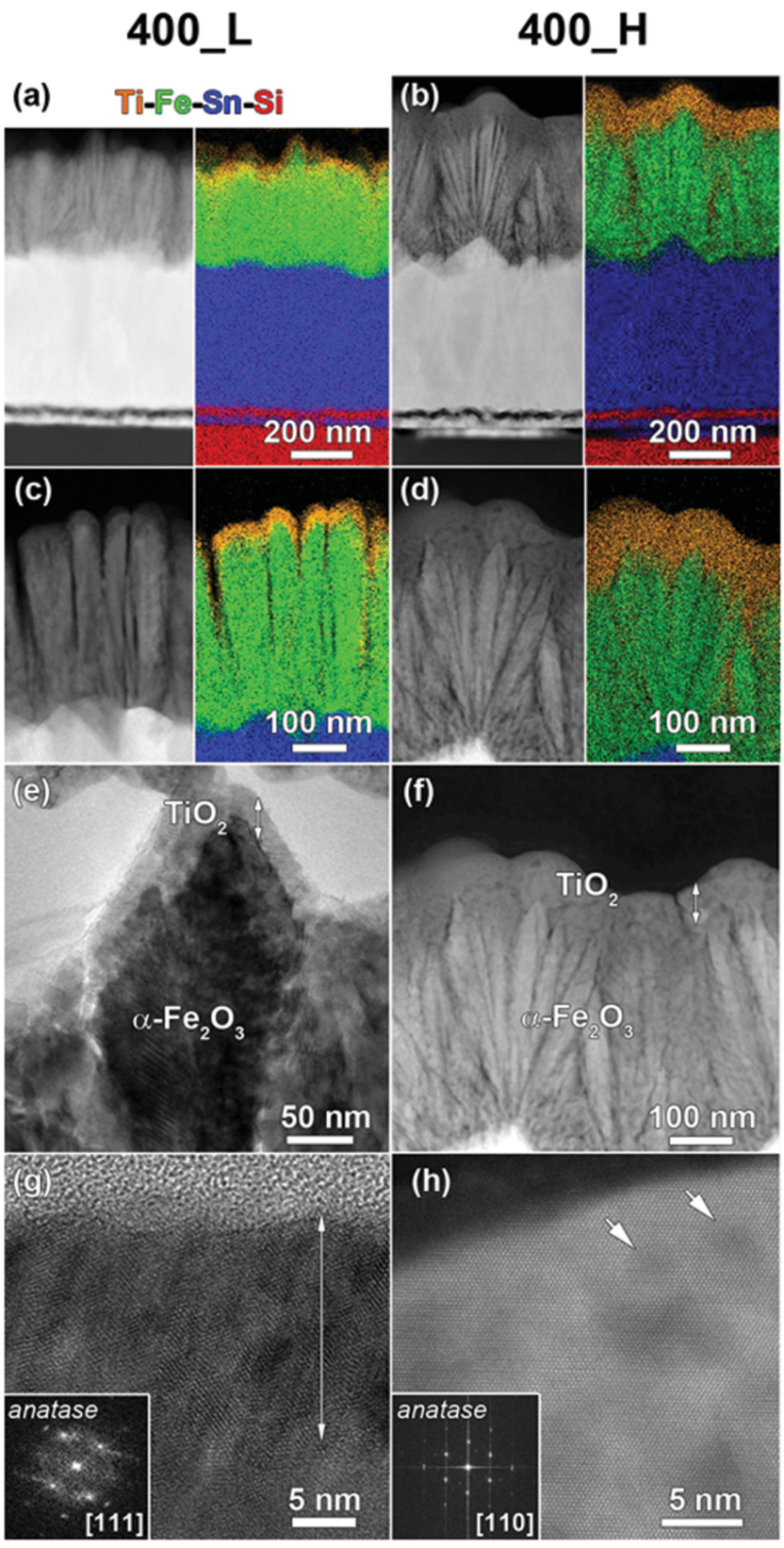

Figure 3. TEM characterization of Fe_2O_3–TiO_2 photoanodes. a–d) Cross sectional HAADF-STEM images and corresponding EDXS chemical maps of samples a,c) 400_L and b,d) 400_H. e) TEM overview image of sample 400_L. f) HAADF-STEM overview of sample 400_H. In both cases, the TiO_2 overlayer thickness is marked by a double-ended arrow. g) HR-TEM image of sample 400_L, evidencing the low crystallinity of the anatase top layer. The anatase layer is imaged along the [111] zone axis, as evidenced by the inset Fourier transform (FT) pattern. h) High resolution HAADF-STEM image of sample 400_H, with arrows indicating the presence of small dark-contrast voids in the highly crystalline anatase overlayer. The anatase layer is imaged along the [110] zone axis, as evidenced by the inset FT pattern.

photocurrent values. Interestingly, a dependence of PEC performances on TiO_2 thickness could be clearly appreciated, since sample 400_H displayed a systematic enhancement of photocurrent values with respect to the 400_L one. In particular, 400_H showed an E_{onset} value as low as 0.8 V_{RHE} and j = 2.0 mA cm^{-2} at 1.23 V_{RHE}, a value nearly ten times higher than that pertaining to pure Fe_2O_3. It is generally accepted that the required overpotential is related to the poor oxygen evolution reaction (OER) kinetics and to the unfavorable conduction band energy position for bare Fe_2O_3.[5,6,19,46] As a consequence, the shift of E_{onset} to more cathodic potentials highlights the beneficial effect exerted by TiO_2 functionalization on the system photoresponse. Along with the onset potential, one of the most important parameters to evaluate photoanode performances is represented by the photocurrent value plateau. In this regard, bare Fe_2O_3 reached a plateau at ≈1.4 V (j ≈ 0.6 mA cm^{-2}), whereas Fe_2O_3–TiO_2 systems did not display any appreciable saturation up to 1.8 V vs. RHE (j ≈ 9.6 mA cm^{-2} for specimen 400_H).

Based on the above observations, the higher photocurrents for samples 400_L and 400_H, as well as the absence of saturation effects at potentials higher than 1.23 V vs. RHE, can be traced back to the formation of Fe_2O_3–TiO_2 heterojunctions, responsible for a more efficient charge carrier separation with respect to bare Fe_2O_3.[5] In particular, at 1.23 V_{RHE}, a j value close to 2.0 mA cm^{-2} was recorded for the 400_H specimen. This photocurrent threshold compares very favorably with the best values reported in the literature for Fe_2O_3–TiO_2 photoelectrodes.[4,6,14,15,19,32,50] Such a result, obtained without the use of any expensive/toxic cocatalyst, is very attractive in view of solar water splitting promoted by Fe_2O_3–TiO_2 materials.

In order to elucidate the role of the TiO_2 overlayer, solar-to-hydrogen (STH) efficiency values were calculated from j–E data. It is worth noting that only a few works in the

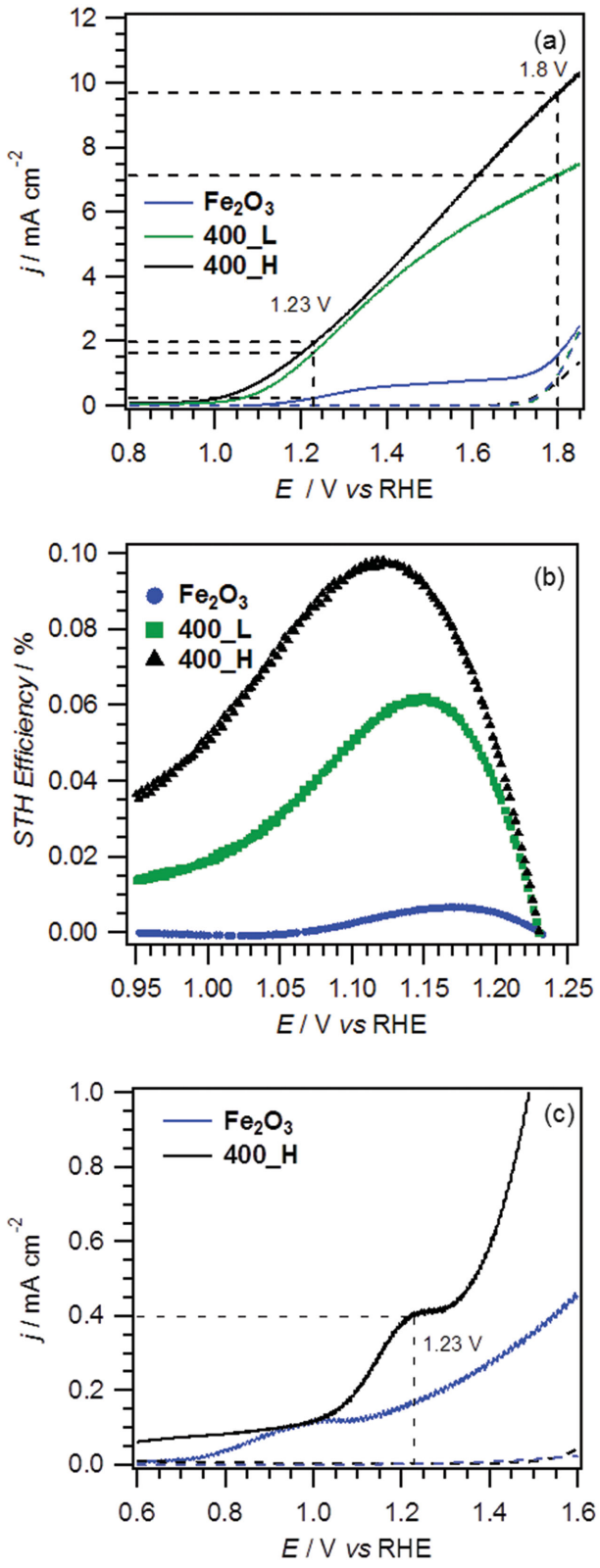

Figure 4. a) Photocurrent density vs. applied potential curves for Fe_2O_3 and Fe_2O_3–TiO_2 photoelectrodes recorded in 1 M NaOH solution under simulated solar irradiation (continuous lines) and in the dark (dashed lines). b) Calculated solar-to-hydrogen (STH) efficiencies. c) *j*–*E* curves for bare Fe_2O_3 and for specimen 400_H in a simulated seawater solution, recorded under solar illumination. Dark current curves are reported as dashed lines.

available literature report STH values for similar systems.[34] As can be appreciated from Figure 4b, the STH efficiency maximum increased in the order: Fe_2O_3 (0.007%) < 400_L (0.060%) < 400_H (0.098%). Notably, the highest photoefficiency values were obtained for TiO_2-containing specimens at *E* values lower than for bare Fe_2O_3. This finding highlights the importance of the Fe_2O_3-TiO_2 heterojunction on charge separation, as well as the positive effect exerted by titania functionalization in enhancing hole dynamics for water oxidation (see also below). To further demonstrate the beneficial role of the Fe_2O_3-TiO_2 heterojunction, it is worth noticing that the PEC response upon solar irradiation (SI, Figure S6) of bare TiO_2, fabricated by ALD and annealed at 650 °C, is almost negligible.

It is well known that the main drawbacks related to the use of Fe_2O_3 photoanodes include the high density of surface states, low hole mobility, short charge-carrier lifetime, and slow OER kinetics.[2,50] On the other hand, even TiO_2 photoanodes suffer from various disadvantages, in particular from poor solar light harvesting.[3,45] So far, some studies have demonstrated that functionalization of Fe_2O_3 with TiO_2 results in worse PEC performances with respect to bare iron(III) oxide.[2,19,50] In a different way, the very high photocurrents shown by the present Fe_2O_3/TiO_2 photoanodes, along with the decreased onset voltages and the absence of significant saturation at high applied potentials, highlight the benefit offered by Fe_2O_3/TiO_2 heterojunctions in affording favorable photoactivity improvements.[3,16,27,47] Due to the mutual positions of Fe_2O_3 and TiO_2 conduction band edges, electrons photogenerated in TiO_2 can be easily transferred to Fe_2O_3 and injected into the FTO substrate, and can subsequently migrate through the external electric circuit to reduce water at the cathode,[45] suppressing thus detrimental recombination effects (see also below and **Scheme 1**). An additional favorable contribution to the actual performances is related to the fact that TiO_2 overlayers can prevent hematite photocorrosion in a wide pH range.[5]

To attain an insight into the stability of the present materials, PEC measurements were carried out under the same conditions at the first and third day of utilization for the best performing system, i.e. specimen 400_H. The obtained experimental results (Figure S7, Supporting Information) revealed that the measured photocurrent values did not undergo any appreciable variation, evidencing a good stability of the target photoanodes, a key prerequisite for their technological applications.

Based on these very favorable results, the most efficient and promising photoelectrode (400_H) was tested in PEC water splitting using simulated seawater solutions. The use of seawater represents a key technological target for a real-world sustainable hydrogen generation, since 97.5% of the overall H_2O available on earth is salt water.[55,56] Figure 4c compares *j*–*E* curves obtained using simulated seawater upon solar illumination for specimen 400_H and for bare Fe_2O_3. As can be observed, for the latter, an increase in photocurrent densities with the applied potential was observed (≈0.2 mA cm^{-2} at 1.23 V_{RHE}). Interestingly, sample 400_H yielded a higher photocurrent density that, despite being lower than that recorded in NaOH solutions (compare Figure 4a), reached *j* values of ≈0.4 mA cm^{-2} at 1.23 V_{RHE}. This result, along with the previously discussed PEC data, shows that the obtained Fe_2O_3–TiO_2 materials represent a key step forward for the fabrication of photoanodes to be used in real-world devices.

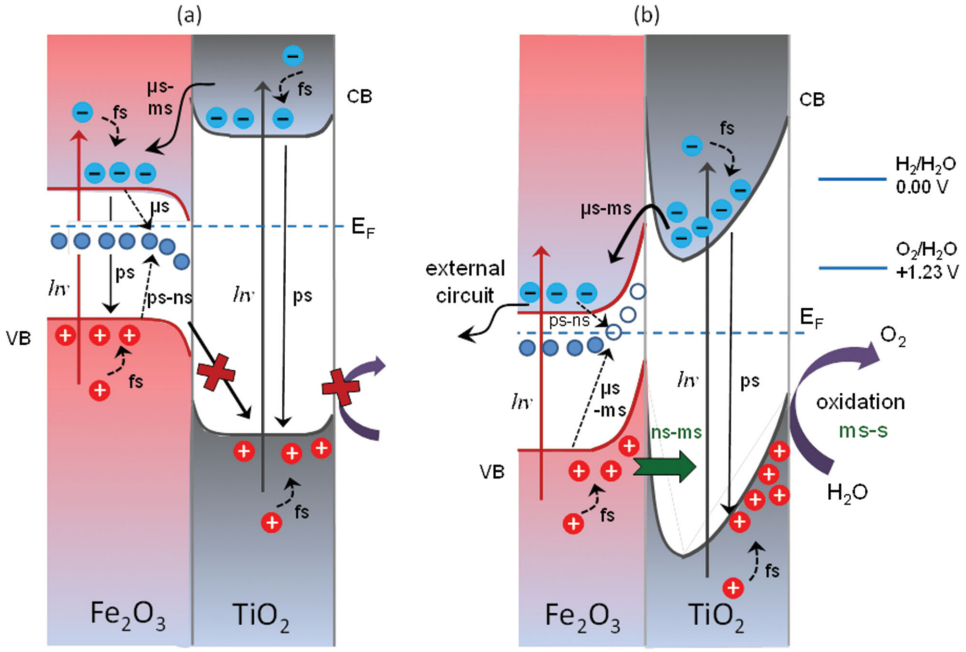

Scheme 1. Schematic energy level diagrams illustrating the photoactivated charge transfer processes and related timescales: a) without and b) with the application of a positive external bias to Fe_2O_3–TiO_2 photoanodes. The intraband electron-trap states, located a few 100 mV below the conduction band edge of hematite, are also shown (CB: conduction band, VB: valence band, E_F: Fermi level, fs: femtosecond, ps: picosecond, ns: nanosecond, μs: microsecond, ms: millisecond).

2.3. TAS Analysis on Fe_2O_3–TiO_2 Photoanodes

To further elucidate the role of Fe_2O_3/TiO_2 heterojunctions in promoting the PEC water splitting and investigate charge-carrier dynamics in the target photoelectrodes, transient absorption spectroscopy (TAS) analyses were carried out. TAS measurements allow the monitoring of photogenerated electron and hole dynamics from a picosecond to a second timescale,[57–59] and are a powerful tool for the study of the interplay between nanostructure and PEC response in Fe_2O_3 and TiO_2 based photoanodes.[25,42,57,60,61] In this work, the evolution of charge carriers was examined by using band-gap excitation of both Fe_2O_3 and TiO_2 at λ = 355 nm, simulating the solar illumination conditions in which light is absorbed by both components.

To investigate the electron mobility of TiO_2 functionalized specimens, microsecond-to-millisecond TAS decays were measured at λ = 580 nm. The selected probe wavelength corresponds to electrons trapped in hematite intra-band states and long-lived holes in both hematite and anatase.[57,58,62] Transient absorption traces and corresponding exponential fits for the specimens are displayed in **Figure 5**a. The initial photobleaching, i.e., the negative absorption change, following the excitation laser pulse could be assigned to the intra-band trapped electrons in hematite.[57] The fits resulted in lifetimes of 1.7 and 900 ms for bare Fe_2O_3, 0.5 and 550 ms for sample 400_L, and 0.3 and 330 ms for sample 400_H, respectively. The short-lived components correspond to the bleaching recovery, attributed to the extraction of trapped electrons, and are therefore indicative of electron mobility in the metal oxide structure. The increased bleaching recovery rate ($1/\tau$) of 400_L and 400_H with respect to bare Fe_2O_3 suggests enhanced electron mobility for the Fe_2O_3–TiO_2 heterostructure. TAS amplitude for 400_L and 400_H is higher with respect to bare Fe_2O_3 (Figure 5a), indicating therefore a higher amount of holes surviving the initial electron–hole recombination in the TiO_2 functionalized photoanodes. The long-lived components with the positive absorption were assigned to holes participating to water oxidation, and were resolved more accurately in a millisecond-to-second timescale (see below) in which water splitting has been reported to occur.[57,63]

The TAS decays of the specimens in a second time range and at a probe wavelength of λ = 650 nm, corresponding to the hole absorption in both Fe_2O_3 and TiO_2,[58,62] were fitted with an exponential model, shown in Figure 5b (see also Figure S8, Supporting Information). Functionalization of Fe_2O_3 with TiO_2 decreased the lifetime of long-lived photoholes, as indicated by the mean lifetimes of 3.0 and 1.8 s obtained for the bare Fe_2O_3 and 400_L photoanodes, respectively. This phenomenon is in good agreement with the higher PEC response of the TiO_2 containing specimens, as it demonstrates an enhanced water oxidation reaction rate. Previously published hole lifetimes for water oxidation over TiO_2 photoelectrodes were close to 0.3 s.[61,63] Hence, despite the presence of the TiO_2 overlayer, hole dynamics of specimen 400_L are directly influenced by the presence of the underlying hematite. Moreover, a photohole lifetime of 0.5 s was obtained for specimen 400_H (Figure 5b), close to the above literature value for bare TiO_2. The decreased photohole lifetime for 400_H with respect to bare Fe_2O_3 and 400_L is noticeable already on a millisecond timescale in Figure 5. The uniform and thicker coverage of Fe_2O_3 by TiO_2 in specimen 400_H can likely be considered responsible for the similar hole lifetimes as published perviously for pure TiO_2. The faster surface reaction kinetics with the thicker TiO_2

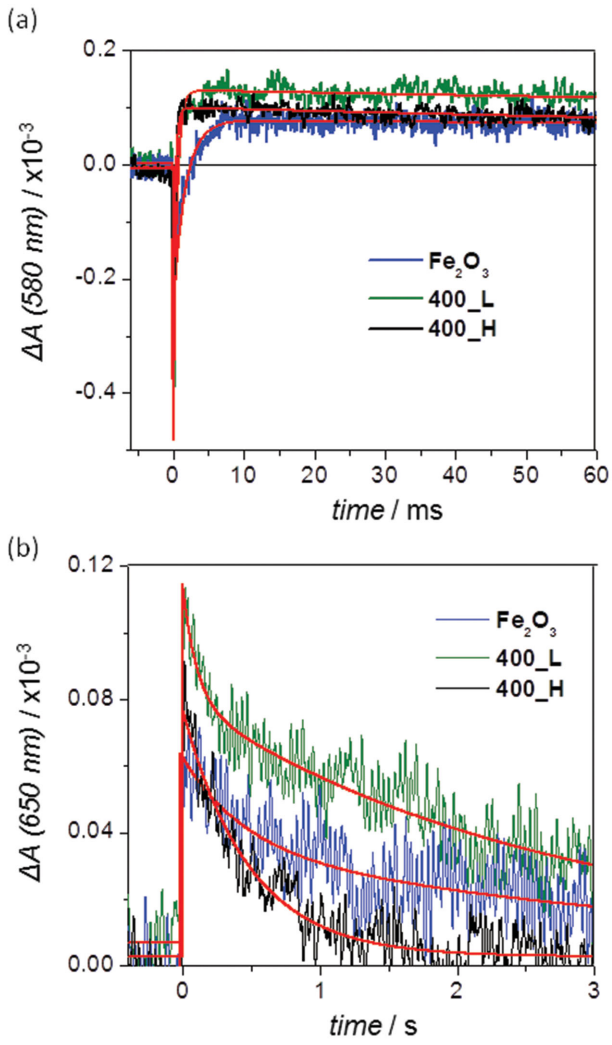

Figure 5. TAS decays for bare Fe_2O_3 and Fe_2O_3–TiO_2 samples on a) a millisecond and b) a second timescale. Red lines represent exponential fits of raw data.

overlayer directly explains the higher PEC response of this photoanode in comparison to the 400_L one, overcoming the slow OER kinetics typical for Fe_2O_3.

Picosecond TAS decays for the bare Fe_2O_3, 400_L, and 400_H photoanodes were compared at 580 nm to investigate the effect of TiO_2 functionalization on initial electron–hole recombination in Fe_2O_3. The retarded electron–hole recombination on the <10 ps time range for the Fe_2O_3–TiO_2 specimens (Figure S9, Supporting Information) was assigned to the passivation of Fe_2O_3 surface defects by TiO_2 deposition,[6] favoring, in turn, a decrease in detrimental charge recombination events.

To rationalize the obtained data, it is necessary to consider that the lower valence band energy of TiO_2 with respect to Fe_2O_3 potentially prohibits hole transfer from Fe_2O_3 to TiO_2,[64] and this phenomenon should lead to a decreased PEC response. However, as demonstrated by Figure 4 and the related discussion, the photocurrent response of TiO_2 functionalized specimens (400_L and 400_H) significantly outperforms that of the bare hematite (Fe_2O_3). Such a remarkable PEC enhancement suggests an efficient charge carrier separation upon coupling the two components in the resulting Fe_2O_3–TiO_2 photoelectrodes. In particular, the role of the junction can be illustrated by analyzing the energy band diagram presented in Scheme 1a,b without and with applied external bias.[24,57,58,65] The system Fermi level energy is lowered with increasing positive bias, which further promotes band bending at the interfaces, an effect that becomes more pronounced upon raising the applied potential. We propose that high photocurrents are achieved only after the valence band energy of hematite shifts to lower values with respect to the TiO_2 valence band edge at the electrolyte interface, promoting thus hole transfer from Fe_2O_3 to TiO_2. This conclusion is supported by the fact that no photocurrent plateau was observed for the TiO_2 functionalized specimens (Figure 4), attributed to enhanced driving force for hole transfer through TiO_2 with respect to increasing anodic potential that further promotes band bending (Scheme 1). In addition, hole conduction from Fe_2O_3 to titania via TiO_2 electronic defect states can be considered as a possible alternative hole transport mechanism.[24]

On the basis of these results, the high PEC response for the TiO_2 functionalized specimens are due to: i) formation of the Fe_2O_3-TiO_2 heterojunction promoting charge separation, and ii) enhanced hole dynamics for water oxidation due to titania overlayer functionalization. In addition, band bending, becoming more important upon raising the applied external bias, further enhances spatial charge separation by hole transport through the TiO_2 overlayer (Scheme 1b).

3. Conclusions

In conclusion, we have successfully prepared Fe_2O_3–TiO_2 nanoheterostructure photoanodes on FTO by the initial PE-CVD growth of Fe_2O_3 nanosystems followed by ALD of TiO_2 layers with variable thickness and final annealing in air. The inherent benefits of the adopted joint process have enabled the fabrication of high-purity systems, characterized by an intimate contact between Fe_2O_3 and TiO_2. These features synergistically contributed to the extremely high performances in photoelectrochemical water oxidation activated by solar illumination, which corresponded to ≈2.0 mA cm^{-2} photocurrent density at 1.23 V vs. RHE under simulated one-sun irradiation. The significant amplification in the PEC performance with respect to the case of bare Fe_2O_3 was mainly attributed to the beneficial role of Fe_2O_3–TiO_2 heterojunctions, resulting in an enhanced charge separation and retarded electron–hole recombination. In addition, TiO_2 protective action against corrosion has enabled the obtainment of attractive preliminary results even for PEC tests in seawater, whose use in solar water splitting is reported for the first time for Fe_2O_3–TiO_2 systems. These results, along with the high and stable photoanode activity, pave the way to sustainable energy generation starting from abundant and renewable natural resources through cost-effective nano-heterostructure devices. The proposed strategy and, in particular, the surface functionalization using ALD-deposited layers, may open doors to the use of combined synthesis approaches in the fabrication of a variety of nanostructures for photoassisted applications displaying improved functionalities.

Based on the present data, optimization of the material performances will require a fine tailoring of Fe_2O_3 morphology to obtain nanosystems endowed with higher porosity, and the investigation of higher TiO_2 loadings on such materials and on the ultimate functional behavior. Furthermore, detailed studies on the properties of the developed systems by incident photon-to-current efficiency, external quantum efficiency, and impedance spectroscopy analyses will also be performed, in order to attain a detailed insight on the heterojunction properties.

4. Experimental Section

4.1. Synthesis

Fe_2O_3 nanodeposits were fabricated using a custom-built two-electrode PE-CVD apparatus [radio frequency (RF) = 13.56 MHz; electrode diameter = 9 cm; interelectrode distance = 6 cm].[41] Depositions were performed on previously cleaned[41,66] FTO-coated glass substrates (Aldrich, 735167-1EA, ≈7 Ω sq^{-1}; lateral dimensions = 2.0 × 1.0 cm; FTO thickness ≈600 nm). Iron(III) oxide systems were prepared starting from $Fe(hfa)_2TMEDA$ (hfa = 1,1,1,5,5,5–hexafluoro–2,4–pentanedionate; TMEDA = *N,N,N′,N′*–tetramethylethylenediamine).[67] In a typical growth experiment, 0.30 ± 0.01 g of precursor powders were placed in an external glass reservoir, heated by an oil bath at 65 °C, and transported into the reaction chamber by electronic grade Ar [flow rate = 60 standard cubic centimeters per minute (sccm)]. In order to prevent undesired precursor condensation phenomena, connecting gas lines were maintained at 140 °C by means of external heating tapes. Two additional gas inlets were used for the independent introduction of electronic grade Ar and O_2 (flow rates = 15 and 20 sccm, respectively) directly into the reaction chamber. After preliminary optimization experiments, each deposition was carried out for 1 h under the following conditions: growth temperature = 400 °C; total reactor pressure = 1.0 mbar; RF-power of 10 W.

The as-prepared Fe_2O_3 nanodeposits were subsequently coated with TiO_2 layers of different thicknesses by means of ALD. ALD experiments were performed at a deposition temperature of 150 °C by a Ultratech/Cambridge Nanotech Inc. Savanna 100 machine operating between 13–15 mbar in continuous flow mode at 20 sccm. Titanium oxide was deposited starting from titanium(IV) tetraisopropoxide [$Ti(O^iPr)_4$] and milliQ water (H_2O) as Ti and O sources, respectively. $Ti(O^iPr)_4$ was purchased from STREM Chemicals, Inc. (France) and used without any further purification. MilliQ water was produced by means of a Millipore DirectQ-5 purification system starting from tap water. The precursors were injected in the reactor directly from stainless steel reservoirs maintained at 80 °C [$Ti(O^iPr)_4$] and 25 °C (H_2O). Electronic grade N_2 was used as carrier to feed the precursor vapors alternatively into the reaction chamber. To avoid precursor condensation, both valves and delivery lines were maintained at 115 °C. After an initial prescreening of the operating conditions, the use of thicker titania overlayers has been intentionally discarded in order to prevent the obtainment of too compact systems with reduced active area, a feature that could detrimentally affect the ultimate functional performances. After this optimization process, the cycle numbers were selected (Table 1) in order to obtain TiO_2 overlayers with the desired thickness.

After deposition, thermal treatments were carried out in air for 1 h at atmospheric pressure using a Carbolite HST 12/200 tubular furnace (heating rate = 20 °C min^{-1}) at 650 °C. The use of higher temperatures was discarded, to prevent detrimental thermal degradations of FTO substrates.[43]

4.2. Characterization

FE-SEM analyses were carried out using a Zeiss SUPRA 40 VP FE-SEM instrument equipped with an Oxford INCA X-sight X-ray detector for EDXS investigation, operating at primary beam acceleration voltages comprised between 10.0 and 20.0 kV.

AFM analyses were run using an NT-MDT SPM solver P47H-PRO instrument operating in semicontact/tapping mode and in air. After plane fitting, RMS roughness values were obtained from 3 × 3 μm^2 images.

SIMS investigation was performed by means of an IMS 4f mass spectrometer (Cameca) using a Cs^+ primary beam (voltage = 14.5 keV; current = 25 nA; stability = 0.2%) and negative secondary ion detection, adopting an electron gun for charge compensation. Beam blanking mode and high mass resolution configuration were adopted. Signals were recorded rastering over a 150 × 150 μm^2 area and detecting secondary ions from a subregion close to 10 × 10 μm^2 in order to avoid crater effects.

XRD measurements were conducted operating in reflection mode by means of a Dymax-RAPID microdiffractometer equipped with a cylindrical imaging plate detector, allowing data collection from 0° to 160° (2θ) horizontally and from −45° to +45° (2θ) vertically upon using CuKα radiation (λ = 1.54056 Å). Each pattern was collected with an exposure time of 40 min, using a collimator diameter of 300 μm. Conventional XRD patterns were obtained by integration of 2D images.

TEM, HAADF-STEM, and EDXS mapping experiments were carried out on a FEI Tecnai Osiris microscope, operated at 200 kV and equipped with a Super-X high solid angle energy-dispersive X-ray detector, as well as a FEI Titan "cubed" microscope (acceleration voltage = 200 kV), equipped with an aberration corrector for the probe-forming lens and a Super-X high solid angle EDXS detector.

XPS analyses were run on a Perkin–Elmer Φ 5600ci apparatus with a standard AlKα radiation (hν = 1486.6 eV), at operating pressures <10^{-8} mbar. Charge correction was performed by assigning to the adventitious C1s signal a Binding Energy (BE) of 284.8 eV.[68] After a Shirley-type background subtraction, atomic percentages (at%) were calculated by signal integration using standard PHI V5.4A sensitivity factors.

Optical absorption spectra were recorded in transmission mode at normal incidence by means of a Cary 50 spectrophotometer, using bare FTO glass as a reference. In all cases, the substrate contribution was subtracted. Tauc plots were determined based on the Tauc equation, assuming the occurrence of direct allowed transitions.[41,43]

PEC measurements were performed in unbuffered 1 M NaOH solutions and, for selected systems, in simulated sea water (35 g L^{-1} sea salt from Tropic Marin), using a saturated calomel electrode (SCE) as reference, a Pt wire as counter-electrode and the Fe_2O_3–TiO_2 nanodeposits as working electrodes. A copper wire was soldered on an uncovered portion of the FTO substrate to establish electrical connection, and an epoxy resin was used to seal all exposed FTO portions, except for the electrode working areas.[69] Prior to measurements, the electrolyte was purged with N_2 to prevent any possible reaction with dissolved O_2. Linear sweep voltammetry (10 mV s^{-1}) was carried out between −1.0 and 1.0 V vs. SCE using a potentiostat (PAR, Versa state IV), both in the dark and under front side illumination, using a Xe lamp (150 W, Oriel) with an AM 1.5 filter. Potentials with respect to the RHE scale (E_{RHE}) were calculated using the Nernst equation.[35]

$$E_{RHE} = E_{SCE} + E^0_{SCE} + 0.059\text{pH} \quad (1)$$

where E_{SCE} and E^0_{SCE} are the actual and standard potentials against SCE.

STH efficiency values are calculated based on the following equation[5,34]

$$\text{STH efficiency}(\%) = j \times (1.23 - E_{RHE}) / I_{light} \quad (2)$$

where E_{RHE} is the applied bias vs. RHE and I_{light} denotes the irradiance intensity (equal to 100 mW cm^{-2} for AM 1.5G illumination).

TAS experiments were performed on photoanodes having a geometric area of 3 × 3 cm^2 in a three-electrode PEC cell (Zahner-elektrik PECC-2) with a Pt counter-electrode, an Ag/AgCl (3 M KCl) reference electrode, and 0.1 M NaOH electrolyte (degassed with N_2 prior to measurements). A potential value of 1.6 V vs. RHE was controlled by a

standard potentiostat (CompactStat, Ivium Technologies) to probe the charge dynamics under water splitting conditions. TAS measurements in a microsecond-to-second timescale were carried out by a modified flash-photolysis apparatus (Luzchem LFP-111) with a New Focus (model 2051) photodetector and a halogen lamp (9 W, Thorlabs SLS201/M) probe. The excitation was fixed at $\lambda = 355$ nm, with an energy density of 0.4 mJ cm^{-2}. The transient absorption traces were averaged 50–80 times. The microsecond-to-second decays are smoothed by using the Savitzky–Golay method with 25 smoothing point.

The picosecond-to-nanosecond TAS experiments were performed by a pump-probe system consisting of Libra F-1K (Coherent Inc.) generator producing 100 fs pulses at λ = 800 nm (1 mJ) with a repetition rate of 1 kHz.[70] An optical parametric amplifier (Topas-C, Light Conversion Ltd.) was used to provide pump pulses at $\lambda = 355$ nm. The measuring component was ExciPro (CDP Inc.) equipped with two array photodetectors coupled with a spectrometer (CDP2022i) set for probe detection in the 500–700 nm interval, with averaging over 10 000 excitation shots. The maximum time range available for probing was ≈6 ns. TAS decays were fitted by using exponential functions in order to elucidate the charge transfer processes and corresponding timescales in the studied photoanode systems.

Supporting Information

Supporting Information is available from the Wiley Online Library or from the author.

Acknowledgements

The authors kindly acknowledge the financial support under the FP7 project "SOLAROGENIX" (NMP4-SL-2012-310333), as well as Padova University ex-60% 2012–2014 projects, Grant No. CPDR132937/13 (SOLLEONE), and Regione Lombardia-INSTM ATLANTE projects. S.T. acknowledges the FWO Flanders for a postdoctoral scholarship.

Received: June 12, 2015
Revised: July 24, 2015
Published online:

[1] S. J. A. Moniz, S. A. Shevlin, D. J. Martin, Z.-X. Guo, J. Tang, *Energy Environ. Sci.* **2015**, *8*, 731.
[2] R. Liu, Z. Zheng, J. Spurgeon, X. Yang, *Energy Environ. Sci.* **2014**, *7*, 2504.
[3] W. H. Hung, T. M. Chien, A. Y. Lo, C. M. Tseng, D. D. Li, *RSC Adv.* **2014**, *4*, 45710.
[4] P. Luan, M. Xie, X. Fu, Y. Qu, X. Sun, L. Jing, *Phys. Chem. Chem. Phys.* **2015**, *17*, 5043.
[5] S. Hernández, V. Cauda, D. Hidalgo, V. Farías Rivera, D. Manfredi, A. Chiodoni, F. C. Pirri, *J. Alloys Compd.* **2014**, *615*, S530.
[6] X. Yang, R. Liu, C. Du, P. Dai, Z. Zheng, D. Wang, *ACS Appl. Mater. Interfaces* **2014**, *6*, 12005.
[7] M. Rioult, H. Magnan, D. Stanescu, A. Barbier, *J. Phys. Chem. C* **2014**, *118*, 3007.
[8] D. Barreca, G. Carraro, V. Gombac, A. Gasparotto, C. Maccato, P. Fornasiero, E. Tondello, *Adv. Funct. Mater.* **2011**, *21*, 2611.
[9] G. Carraro, C. Maccato, A. Gasparotto, T. Montini, S. Turner, O. I. Lebedev, V. Gombac, G. Adami, G. Van Tendeloo, D. Barreca, P. Fornasiero, *Adv. Funct. Mater.* **2014**, *24*, 372.
[10] D. P. Cao, W. J. Luo, J. Y. Feng, X. Zhao, Z. S. Li, Z. G. Zou, *Energy Environ. Sci.* **2014**, *7*, 752.
[11] G. K. Mor, H. E. Prakasam, O. K. Varghese, K. Shankar, C. A. Grimes, *Nano Lett.* **2007**, *7*, 2356.
[12] L. Wang, C. Y. Lee, P. Schmuki, *Electrochem. Commun.* **2013**, *30*, 21.
[13] X. J. Lian, X. Yang, S. J. Liu, Y. Xu, C. P. Jiang, J. W. Chen, R. L. Wang, *Appl. Surf. Sci.* **2012**, *258*, 2307.
[14] C. X. Kronawitter, Z. Ma, D. Liu, S. S. Mao, B. R. Antoun, *Adv. Energy Mater.* **2012**, *2*, 52.
[15] J. H. Kim, J. H. Kim, J.-W. Jang, J. Y. Kim, S. H. Choi, G. Magesh, J. Lee, J. S. Lee, *Adv. Energy Mater.* **2015**, *5*, 1401933.
[16] P. Luan, M. Xie, D. Liu, X. Fu, L. Jing, *Sci. Rep.* **2014**, *4*, 6180.
[17] O. Zandi, B. M. Klahr, T. W. Hamann, *Energy Environ. Sci.* **2013**, *6*, 634.
[18] B. Klahr, S. Gimenez, F. Fabregat-Santiago, T. Hamann, J. Bisquert, *J. Am. Chem. Soc.* **2012**, *134*, 4294.
[19] F. Le Formal, N. Tetreault, M. Cornuz, T. Moehl, M. Grätzel, K. Sivula, *Chem. Sci.* **2011**, *2*, 737.
[20] L. Steier, I. Herraiz-Cardona, S. Gimenez, F. Fabregat-Santiago, J. Bisquert, S. D. Tilley, M. Grätzel, *Adv. Funct. Mater.* **2014**, *24*, 7681.
[21] H. Magnan, D. Stanescu, M. Rioult, E. Fonda, A. Barbier, *Appl. Phys. Lett.* **2012**, *101*, 133908.
[22] S. Li, P. Zhang, X. Song, L. Gao, *Int. J. Hydrogen Energy* **2014**, *39*, 14596.
[23] F. Le Formal, M. Grätzel, K. Sivula, *Adv. Funct. Mater.* **2010**, *20*, 1099.
[24] S. Hu, M. R. Shaner, J. A. Beardslee, M. Lichterman, B. S. Brunschwig, N. S. Lewis, *Science* **2014**, *344*, 1005.
[25] D. A. Wheeler, G. Wang, Y. Ling, Y. Li, J. Z. Zhang, *Energy Environ. Sci.* **2012**, *5*, 6682.
[26] G. M. Carroll, D. K. Zhong, D. R. Gamelin, *Energy Environ. Sci.* **2015**, *8*, 577.
[27] W.-H. Hung, T.-M. Chien, C.-M. Tseng, *J. Phys. Chem. C* **2014**, *118*, 12676.
[28] D. Wang, X.-T. Zhang, P.-P. Sun, S. Lu, L.-L. Wang, Y.-A. Wei, Y.-C. Liu, *Int. J. Hydrogen Energy* **2014**, *39*, 16212.
[29] C. Zhang, Q. Wu, X. Ke, J. Wang, X. Jin, S. Xue, *Int. J. Hydrogen Energy* **2014**, *39*, 14604.
[30] Q. Yu, X. Meng, T. Wang, P. Li, J. Ye, *Adv. Funct. Mater.* **2015**, *25*, 2686.
[31] M. Marelli, A. Naldoni, A. Minguzzi, M. Allieta, T. Virgili, G. Scavia, S. Recchia, R. Psaro, V. Dal Santo, *ACS Appl. Mater. Interfaces* **2014**, *6*, 11997.
[32] S. C. Warren, K. Voïtchovsky, H. Dotan, C. M. Leroy, M. Cornuz, F. Stellacci, C. Hébert, A. Rothschild, M. Grätzel, *Nat. Mater.* **2013**, *12*, 842.
[33] Y. Lin, S. Zhou, S. W. Sheehan, D. Wang, *J. Am. Chem. Soc.* **2011**, *133*, 2398.
[34] P. Sharma, P. Kumar, D. Deva, R. Shrivastav, S. Dass, V. R. Satsangi, *Int. J. Hydrogen Energy* **2010**, *35*, 10883.
[35] G. Wang, Y. Ling, D. A. Wheeler, K. E. N. George, K. Horsley, C. Heske, J. Z. Zhang, Y. Li, *Nano Lett.* **2011**, *11*, 3503.
[36] N. T. Hahn, C. B. Mullins, *Chem. Mater.* **2010**, *22*, 6474.
[37] N. Mirbagheri, D. Wang, C. Peng, J. Wang, Q. Huang, C. Fan, E. E. Ferapontova, *ACS Catal.* **2014**, *4*, 2006.
[38] Z. Fu, T. Jiang, Z. Liu, D. Wang, L. Wang, T. Xie, *Electrochim. Acta* **2014**, *129*, 358.
[39] L. Xi, S. Y. Chiam, W. F. Mak, P. D. Tran, J. Barber, S. C. J. Loo, L. H. Wong, *Chem. Sci.* **2013**, *4*, 164.
[40] M. H. Lee, J. H. Park, H. S. Han, H. J. Song, I. S. Cho, J. H. Noh, K. S. Hong, *Int. J. Hydrogen Energy* **2014**, *39*, 17501.
[41] D. Barreca, G. Carraro, A. Gasparotto, C. Maccato, C. Sada, A. P. Singh, S. Mathur, A. Mettenbörger, E. Bontempi, L. E. Depero, *Int. J. Hydrogen Energy* **2013**, *38*, 14189.
[42] S. Shen, C. X. Kronawitter, D. A. Wheeler, P. Guo, S. A. Lindley, J. Jiang, J. Z. Zhang, L. Guo, S. S. Mao, *J. Mater. Chem. A* **2013**, *1*, 14498.

[43] M. E. A. Warwick, K. Kaunisto, D. Barreca, G. Carraro, A. Gasparotto, C. Maccato, E. Bontempi, C. Sada, T.-P. Ruoko, S. Turner, G. Van Tendeloo, *ACS Appl. Mater. Interfaces* **2015**, *7*, 8667.
[44] C. H. Miao, T. F. Shi, G. P. Xu, S. L. Ji, C. H. Ye, *ACS Appl. Mater. Interfaces* **2013**, *5*, 1310.
[45] S. J. A. Moniz, S. A. Shevlin, X. An, Z.-X. Guo, J. Tang, *Chem. Eur. J.* **2014**, *20*, 15571.
[46] M. T. Mayer, Y. Lin, G. Yuan, D. Wang, *Acc. Chem. Res.* **2013**, *46*, 1558.
[47] C. X. Kronawitter, L. Vayssieres, S. Shen, L. Guo, D. A. Wheeler, J. Z. Zhang, B. R. Antoun, S. S. Mao, *Energy Environ. Sci.* **2011**, *4*, 3889.
[48] J. Y. Kim, G. Magesh, D. H. Youn, J.-W. Jang, J. Kubota, K. Domen, J. S. Lee, *Sci. Rep.* **2013**, *3*, 2681.
[49] D. Barreca, G. Carraro, A. Gasparotto, C. Maccato, F. Rossi, G. Salviati, M. Tallarida, C. Das, F. Fresno, D. Korte, U. L. Stangar, M. Franko, D. Schmeisser, *ACS Appl. Mater. Interfaces* **2013**, *5*, 7130.
[50] Z. Li, W. Luo, M. Zhang, J. Feng, Z. Zou, *Energy Environ. Sci.* **2013**, *6*, 347.
[51] Y. Ling, G. Wang, D. A. Wheeler, J. Z. Zhang, Y. Li, *Nano Lett.* **2011**, *11*, 2119.
[52] J. Luo, X. Xia, Y. Luo, C. Guan, J. Liu, X. Qi, C. F. Ng, T. Yu, H. Zhang, H. J. Fan, *Adv. Energy Mater.* **2013**, *3*, 737.
[53] Pattern N° 33–0664, JCPDS (2000).
[54] Pattern N° 00–021–1272, JCPDS (2000).
[55] S. M. Ji, H. Jun, J. S. Jang, H. C. Son, P. H. Borse, J. S. Lee, *J. Photochem. Photobiol., A* **2007**, *189*, 141.
[56] H. Joo, S. Bae, C. Kim, S. Kim, J. Yoon, *Sol. Energy Mater. Sol. Cells* **2009**, *93*, 1555.
[57] M. Barroso, S. R. Pendlebury, A. J. Cowan, J. R. Durrant, *Chem. Sci.* **2013**, *4*, 2724.
[58] S. R. Pendlebury, X. Wang, F. Le Formal, M. Cornuz, A. Kafizas, S. D. Tilley, M. Grätzel, J. R. Durrant, *J. Am. Chem. Soc.* **2014**, *136*, 9854.
[59] B. C. Fitzmorris, J. M. Patete, J. Smith, X. Mascorro, S. Adams, S. S. Wong, J. Z. Zhang, *ChemSusChem* **2013**, *6*, 1907.
[60] A. J. Cowan, W. Leng, P. R. F. Barnes, D. R. Klug, J. R. Durrant, *Phys. Chem. Chem. Phys.* **2013**, *15*, 8772.
[61] J. Tang, J. R. Durrant, D. R. Klug, *J. Am. Chem. Soc.* **2008**, *130*, 13885.
[62] A. J. Cowan, C. J. Barnett, S. R. Pendlebury, M. Barroso, K. Sivula, M. Grätzel, J. R. Durrant, D. R. Klug, *J. Am. Chem. Soc.* **2011**, *133*, 10134.
[63] J. Tang, A. J. Cowan, J. R. Durrant, D. R. Klug, *J. Phys. Chem. C* **2011**, *115*, 3143.
[64] J. B. Baxter, C. Richter, C. A. Schmuttenmaer, *Annu. Rev. Phys. Chem.* **2014**, *65*, 423.
[65] L. Peng, T. Xie, Y. Lu, H. Fan, D. Wang, *Phys. Chem. Chem. Phys.* **2010**, *12*, 8033.
[66] G. Carraro, A. Gasparotto, C. Maccato, E. Bontempi, F. Bilo, D. Peeters, C. Sada, D. Barreca, *Cryst. Eng. Commun.* **2014**, *16*, 8710.
[67] D. Barreca, G. Carraro, A. Devi, E. Fois, A. Gasparotto, R. Seraglia, C. Maccato, C. Sada, G. Tabacchi, E. Tondello, A. Venzo, M. Winter, *Dalton Trans.* **2012**, *41*, 149.
[68] D. Briggs, M. P. Seah, *Practical Surface Analysis: Auger and X-ray Photoelectron Spectroscopy*, 2nd ed., John Wiley and Sons, New York **1990**.
[69] S. Kumari, A. P. Singh, Sonal, D. Deva, R. Shrivastav, S. Dass, V. R. Satsangi, *Int. J. Hydrogen Energy* **2010**, *35*, 3985.
[70] D. Sirbu, C. Turta, A. C. Benniston, F. Abou-Chahine, H. Lemmetyinen, N. V. Tkachenko, C. Wood, E. Gibson, *RSC Adv.* **2014**, *4*, 22733.